Coarse-grained simulation of amphiphilic self-assembly

MICHEL, D. J. and CLEAVER, D. J. <http://orcid.org/0000-0002-4278-0098>

Coarse-grained simulation of amphiphilic self-assembly

David J. Michel and Douglas J. Cleaver

Materials Research Institute, Sheffield Hallam University, Pond Street, Sheffield S1 1WB, United Kingdom.

Abstract

We present a computer simulation study of amphiphilic self assembly performed using a computationally efficient single-site model based on Gay-Berne and Lennard-Jones particles. Molecular dynamics simulations of these systems show that free self-assembly of micellar, bilayer and inverse micelle arrangements can be readily achieved for a single model parameterisation. This self-assembly is predominantly driven by the anisotropy of the amphiphile-solvent interaction, amphiphile-amphiphile interactions being found to be of secondary importance. While amphiphile concentration is the main determinant of phase stability, molecular parameters such as headgroup size and interaction strength also have measurable affects on system properties.

1 Introduction

Amphiphilic molecules such as surfactants, block copolymers and phospholipids are well known to spontaneously self-assemble into a wide variety of structures when mixed in an aqueous solvent [1, 2]. The formation of these aggregates is substantially attributable to the amphiphilic duality of these molecules, i.e., the fact that they contain both hydrophilic and hydrophobic moieties. The hydrophobic effect is commonly cited as being the main driver of this self-assembly, the amphiphilic molecules tending to aggregate in structures that shield their hydrophobic regions from the aqueous solvent. The resultant structures include micelles, lamellae and the closed bilayer vesicles which are important for nano-biotechnology applications. The mechanisms and processes controlling amphiphilic self-assembly are relevant to sectors ranging from chemical processing to biochemistry and medical interest. Gaining predictive understanding, at the molecular level, of the self-assembly processes relevant to these many aggregate structures is therefore a fundamental challenge.

In response to this, a number of computational models have now been developed with which to simulate aspects of the complex phase behaviour exhibited by amphiphilic systems. Early Monte Carlo simulations of lattice models were the first such systems to yield information on these self-assembling properties. Pioneered by Larson et al. [3] and Care et al. [4], these models proved capable of simulating several micelles for a few micelle life-times. In parallel with these works on intrinsically simple models, atomistic Molecular Dynamics (MD) simulations were also developed to investigate detailed issues underlying the behaviour of these systems. Atomistically detailed simulation studies of such system have now progressed to the stage where, for example, runs have been performed employing 100,000 particles representing a pure 60Å$\times$ 60Å lipid bilayer patch on time-scales approaching 10 ns [5]. However, most all-atom simulations are performed on pre-assembled structures and, therefore, do not give insight into the self-assembly processes of these systems. Indeed, due to the considerable computational costs associated with such simulations, they still fall well short of the time- and length-scales pertinent to the structural changes and co-operative effects associated with biological processes. Thus, while the

self-assembly of surfactants into micelles has been reported by Maillet et al. [6], the length-scale available to these simulations restricted them to only a single micelle and it was not possible to access the dynamic equilibrium processes involved in real micellar behaviour.

In response to these limitations, a series of more generic, coarse-grained (CG) amphiphilic models have been developed to extend the accessible time- and length-scale window. Of these, the model of Marrink et al. [7], which itself is closely related to those previously considered by Lipowsky et al. [8, 9] and Smit et al. [10], is a good example of a simple but very efficient CG model for lipid and surfactant systems. Here, each amphiphilic molecule is represented by a chain of Lennard-Jones beads whose interaction parameters are set to reflect their affinities with one another and with explicit solvent spheres. Through appropriate tuning, these bead-spring models have successfully been used to simulate large time-scale events such as vesicle self-assembly [11], membrane pore formation [12] and vesicle fusion [13]. As an alternative to this scientific-intuition-based approach to parameterising CG models, Shelley et al. [14, 15] have adopted a more prescriptive route. Specifically, they have adopted an approach in which the site-site interactions in a bead-spring-type model have been described by complex tabulated potentials tuned to recover the head group-head group radial distribution function obtained from all-atom simulations of a bilayer structure. While this approach benefits from having no arbitrary parameters, it is questionable whether the resultant potential is transferable to other amphiphilic structures. As such, the predictive capabilities of such a model appear intrinsically limited. In addition to these bead-spring model approaches, in which the aqueous solvent is treated with explicit interaction sites, another class of solvent-free CG models has been developed recently [16–18]. These models have been used to simulate fluid bilayer systems and processes such as vesicle formation. This class of models has proved attractive to the modelling community due to its high computation efficiency. However, most of these models have been designed so as to study specific phases. For example, models developed to simulate the bilayer phase employ a very strong cohesive energy between the amphiphiles, which may preclude the possibility of other amphiphilic phases forming. The neglect of other solvent-mediated effects, such as

hydrodynamics, is also an issue with these models.

All of the models cited thus far are based on assemblies of spherical interaction sites. However, a small number of models have been developed using anisotropic interaction sites based on the Gay-Berne potential [19]. One such model used multiple Gay-Berne sites together with Lennard-Jones sites to form a phospholipid [20]. Another, more coarse-grained, approach used a Gay-Berne site for the solvophobic tail linked with a Lennard-Jones site for the solvophilic head group [21]. Prior to these, a single site Gay-Berne based amphiphilic model was developed in 1989 by Gunn and Dawson [22]. In this model, the amphiphile-solvent interaction was designed so as to create a 'solvophobic-solvophilic' dipole, promoting solvation at just one end of the amphiphilic molecule. This model was parameterised with a very strong side-side interaction, favouring a parallel configuration of the anisotropic sites, *i.e* promoting the formation of a bilayer phase. Unfortunately, relatively little work was performed to investigate the full capabilities of this class of model.

All of the CG models listed above have in common a relatively weak attractive or repulsive tail-solvent interaction compared with the other interactions employed. The self-assembly processes described by these models are, therefore, enthalpic in origin and should be essentially independent of temperature. It is, nevertheless, important to recall that some aspects of the self-assembly of surfactant molecules in aqueous solutions are generally accepted as being entropy-driven processes with clear temperature dependence. One could, therefore, argue that these models are not appropriate for studying these self-assembly phenomena in aqueous solutions. As already noted by Lipowsky *et al.* [8], these enthalpic models could, indeed, correspond better to enthalpy-driven self-assembly in non-polar solvents [23–26]. One could alternatively argue that some degree of entropic rearrangement is actually incorporated into those models via the packing of the solvent around the hydrophobic tail induced by the strong solvent-solvent attraction.

Ultimately, these models balance the mechanisms responsible for the self-assembly (be they entropic or enthalpic) in a way which makes the net free energy change for dissolution un-

favourable. There exisits, thus, a need to examine how sensitive these processes and structures are to the make-up of this balance. To assess this, however, it is necessary to have access to a model capable of exhibiting multiple phases and large time- and length-scale phenomena. In this context, we present here a simulation study of a computationally efficient generic model capable of exhibiting a wide range amphiphilic phase behaviour. In the next section, the model, which is based on the well established Gay-Berne model for thermotropic liquid crystals [19], is described and characterised in terms of basic molecular parameters. Following this, we present results from MD simulations performed with this model for a wide range of amphiphile-solvent compositions. From these, we examine the ability of this model to freely self-assemble into a range of amphiphilic structures including micelles, bilayers and inverse micelles. Finally, we discuss the limitations and capabilities of this model, with a view to assessing its ability to relate molecular parameters such as the hydrophilic-lipophilic balance, hydrophobic strength and molecule shape to amphiphilic phase behaviour and structure-formation processes.

2 Definition of the computer model

Molecular models employed in simulations of thermotropic liquid crystals can, like those summarised in the previous section, be broadly categorised as all-atom based or CG [27]. However, in the field of thermotropics, CG models based on rigid anisotropic units are commonly used. When considered from a molecular basis, this restriction to fixed molecule shape is not obviously justified, given that most mesogens contain significant flexible regions. In practice, though, shape anisotropy has been shown to be a sufficient condition for nematic phase stability, and virtually the full phase behaviour of thermotropic liquid crystals, including a number of different smectic phases, has been obtained without resort to molecular flexibility [27]. While the success of this class of model in this context casts light on the relative importance of different contributions in establishing various phase behaviours, it is also important to recognise an important practical point. Due to their simple and smooth shapes, molecules represented by, e.g., rigid ellipsoids or sphero-cylinders are particularly well-suited to exhibiting phase transitions - due to

their lack of local entanglements and other bottlenecks to structural rearrangement, the phase stability of such models can be established at significantly lower computational cost than that required for similar but flexible models.

One of the most-used CG models in thermotropic liquid crystal simulation is the Gay-Berne model [19, 28, 29]. Here we examine the ability of such a model to exhibit amphiphilicity by studying the behaviour of appropriately tuned Gay-Berne particles immersed in a solvent of Lennard-Jones spheres.

The model employed here is based on a rod-sphere mixture comprising Gay-Berne and Lennard-Jones particles [30, 31]. In a mixture of two different species, one has to deal with 3 interactions: one interaction for each species and a further interaction between the unlike species. Here, we characterise the sphere-sphere interactions via the Lennard-Jones potential, the rod-rod interactions via the Gay-Berne potential and, finally, the rod-sphere interaction via the Generalised Gay-Berne potential.

The sphere-sphere interaction, modelling the solvent-solvent interaction, is then given by:

$$U^{LJ}(r_{ij}) = 4\epsilon_0 \left[\left(\frac{\sigma_0}{r_{ij}} \right)^{12} - \left(\frac{\sigma_0}{r_{ij}} \right)^{6} \right]. \tag{1}$$

The interaction between rod-like particles, describing the amphiphile-amphiphile interaction, is described by the Gay-Berne potential:

$$U^{GB}(\mathbf{r_{ij}}, \hat{\mathbf{u}}_\mathbf{i}, \hat{\mathbf{u}}_\mathbf{j}) = 4\epsilon(\hat{\mathbf{r}}_\mathbf{ij}, \hat{\mathbf{u}}_\mathbf{i}, \hat{\mathbf{u}}_\mathbf{j}) \left[\left(\frac{\sigma_0}{r_{ij} - \sigma(\hat{\mathbf{r}}_\mathbf{ij}, \hat{\mathbf{u}}_\mathbf{i}, \hat{\mathbf{u}}_\mathbf{j}) + \sigma_0} \right)^{12} - \left(\frac{\sigma_0}{r_{ij} - \sigma(\hat{\mathbf{r}}_\mathbf{ij}, \hat{\mathbf{u}}_\mathbf{i}, \hat{\mathbf{u}}_\mathbf{j}) + \sigma_0} \right)^{6} \right], \tag{2}$$

where $\hat{\mathbf{r}}_\mathbf{ij} = \mathbf{r_{ij}}/r_{ij}$ is a unit vector along the intermolecular vector $\mathbf{r_{ij}} = \mathbf{r_i} - \mathbf{r_j}$. $\hat{\mathbf{u}}_\mathbf{i}$ and $\hat{\mathbf{u}}_\mathbf{j}$ are unit vectors describing the orientations of the rod particles. The shape parameter, $\sigma(\hat{\mathbf{r}}_\mathbf{ij}, \hat{\mathbf{u}}_\mathbf{i}, \hat{\mathbf{u}}_\mathbf{j})$, is defined by

$$\sigma(\hat{\mathbf{r}}_\mathbf{ij}, \hat{\mathbf{u}}_\mathbf{i}, \hat{\mathbf{u}}_\mathbf{j}) = \sigma_0 \left[1 - \frac{\chi}{2} \left\{ \frac{(\hat{\mathbf{r}}_\mathbf{ij} \cdot \hat{\mathbf{u}}_\mathbf{i} + \hat{\mathbf{r}}_\mathbf{ij} \cdot \hat{\mathbf{u}}_\mathbf{j})^2}{1 + \chi(\hat{\mathbf{u}}_\mathbf{i} \cdot \hat{\mathbf{u}}_\mathbf{j})} + \frac{(\hat{\mathbf{r}}_\mathbf{ij} \cdot \hat{\mathbf{u}}_\mathbf{i} - \hat{\mathbf{r}}_\mathbf{ij} \cdot \hat{\mathbf{u}}_\mathbf{j})^2}{1 - \chi(\hat{\mathbf{u}}_\mathbf{i} \cdot \hat{\mathbf{u}}_\mathbf{j})} \right\} \right]^{-1/2}. \tag{3}$$

Here, the parameter χ reflects the shape anisotropy of the rod particle and is a function of the rod length to breadth ratio l/d. Thus,

$$\chi = \frac{(l/d)^2 - 1}{(l/d)^2 + 1}. \tag{4}$$

In this study we have set the ratio $l/d = 3$. For the well-depth anisotropy term, we adopt the form

$$\epsilon(\hat{\mathbf{r}}_{\mathbf{ij}}, \hat{\mathbf{u}}_{\mathbf{i}}, \hat{\mathbf{u}}_{\mathbf{j}}) = \epsilon_0 \left[1 - \chi^2 (\hat{\mathbf{u}}_{\mathbf{i}} \cdot \hat{\mathbf{u}}_{\mathbf{j}})^2\right]^{-1/2}. \tag{5}$$

This is simpler than the equivalent term used in most Gay-Berne parameterisations for thermotropic liquid crystals in that it is independent of the intermolecular vector $\hat{\mathbf{r}}_{ij}$. This amphiphile-amphiphile interaction also involves no breaking of the head-tail symmetry. This means that a tail interacts with a head in exactly the same way as with another tail. The assumptions implied by this interaction are, at face value, counterintuitive, since in real amphiphilic molecules the head groups interact differently with different parts of other amphiphilic molecules. However, one of the aims of this study is to find the minimum requirements, in terms of modelling, needed to achieve amphiphilic behaviour. Investigating whether the breaking of this symmetry is a requirement for the formation of lyotropic structures is, then, a central issue in this study.

The amphiphile-solvent interaction, *i.e.* the rod-sphere interaction, is modelled using the Generalised Gay-Berne potential [32] capable of dealing with interactions between unlike particles. In the specific case of rods and spheres, with the sphere diameter set equal to the rod's breadth, the basic form of (2) is used but the shape parameter is now given by:

$$\sigma(\hat{\mathbf{r}}_{\mathbf{ij}}, \hat{\mathbf{u}}_{\mathbf{j}}) = \sigma_0 \left[1 - \chi (\hat{\mathbf{r}}_{\mathbf{ij}} \cdot \hat{\mathbf{u}}_{\mathbf{j}})^2\right]^{-1/2}. \tag{6}$$

This class of model has been studied by Antypov and Cleaver in respect of the effects of spherical additives on thermotropic liquid crystals [30,31]. In this paper, we develop this model further by making the rod-sphere interaction potential amphiphilic. Specifically, we introduce a functional dependence of the well-depth anisotropy on $\hat{\mathbf{u}}_i \cdot \hat{\mathbf{r}}_{ij}$ (see Fig. 1) which makes one rod

end solvophilic and the other solvophobic.

The mathematical function used to achieve this here is an exponential decay, controlled by the parameters A, B and C.

$$\epsilon(\hat{\mathbf{r}}_{\mathbf{ij}}, \hat{\mathbf{u}}_{\mathbf{j}}) = -\epsilon_0 \left[A + B \cdot \exp\left(C \cdot (\hat{\mathbf{r}}_{\mathbf{ij}} \cdot \hat{\mathbf{u}}_{\mathbf{j}})\right)\right]. \tag{7}$$

This form was found to offer some practical advantages over the simple cubic extension to Antypov and Cleaver's model. The parameters A and B describe the well-depth anisotropy of the rod-sphere interaction whereas C controls the sharpness of the curve, i.e. controls the solvophobic to solvophilic ratio H.

In Antypov and Cleaver's model, the well-depth anisotropy of the rod-sphere interaction was expressed using the parameter $\kappa^{'}$ which set the ratio of the well depths experienced at the side and end of the rod (i.e. setting $\kappa^{'} < 1$ promoted accumulation of spheres at the rod ends). For consistency, here we assume $\kappa^{'} \leq 1$ and impose the constraints $\epsilon(\hat{\mathbf{r}}_{\mathbf{ij}} \cdot \hat{\mathbf{u}}_{\mathbf{j}} = +1) = \epsilon_0/\kappa^{'}$ (lyophilic head, more attractive to solvent) and $\epsilon(\hat{\mathbf{r}}_{\mathbf{ij}} \cdot \hat{\mathbf{u}}_{\mathbf{j}} = -1) = \epsilon_0\kappa^{'}$ (lyophobic tail, less attractive to solvent). From these it then follows that A and B are given by

$$A = \kappa^{'} + \left(\kappa^{'} - \frac{1}{\kappa^{'}}\right)\left(\frac{e^C}{e^C - e^{-C}}\right) \tag{8}$$

$$B = \frac{\left(\frac{1}{\kappa^{'}} - \kappa^{'}\right)}{e^C - e^{-C}}. \tag{9}$$

As noted above, the parameter C controls the sharpness of the decay between the two fixed end points. From this, it is then possible to define a solvophobic-to-solvophilic balance using C to set the crossover point between the solvophobic and the solvophilic parts of the model. A numerical value for this crossover can then be defined in terms of x_0 where $\epsilon(\hat{\mathbf{r}}_{\mathbf{ij}} \cdot \hat{\mathbf{u}}_{\mathbf{j}} = x_0) = \epsilon_0$ and $-1 < x_0 < +1$. Rewriting this in terms of conventional hydrophilic-lipophylic balance language, we then define

$$H = 50(1 + x_0) = 50 \cdot \left(1 + \frac{1}{C} \cdot \ln\left(\frac{(1-A}{B}\right)\right) \tag{10}$$

where H can vary from 0 to 100% and corresponds to the relative size of the solvophobic region compared to the total length of the rod. Note that while Eqn. (10) cannot be analytically inverted to give C as a function of H, numerical inversion is always possible. Fig. 2(a) shows plots of C vs. H for different values of $1/\kappa^{'}$. A comparison between two alternative parameterisations of this model and the original definition of Antypov's model is shown in Fig. 2(b). The H=80% parameterisation shows a relatively sharp transition from the solvophobic region ($\epsilon < 1$) to the solvophilic region ($\epsilon > 1$) compared with that of the H=50% parameterisation. The difference with Antypov's original model can be observed in Fig. 3 which shows equipotential contour plots for the two models. In this, while Antypov's model treats both ends of the rod as being equally attractive, the new formulation has broken this symmetry and only posesses one attractive end.

The model just described represents a very simple representation of an amphiphilc molecule. As noted above, it largely neglects details of the solvent-solvent and amphiphile-amphiphile interactions, implementing these using the simplest volume-conserving potentials available. For simplicity, these interactions are kept identical for all of the systems studied in this paper. The amphiphile-solvent interactions are then characterised by two parameters: the strength anisotropy $\kappa^{'}$, which sets the depth of the attractive minimum at the head end of the amphiphile, and the solvophobic to solvophilic ratio H which determines the extent of the headgroup. Both of these parameters can be expected to affect the inherent curvature of any assemblies formed by these systems, but their precise roles may be expected to differ. The other variable that we shall be considering here is the amphiphile:solvent concentration ratio.

In the next section, we present details of our simulation methodolgy, followed by three sets of simulation results obtained using this model. In the first of these, we examine the effect of concentration on phase behaviour for fixed amphiphile-solvent parameterisation. Following this, we investigate the sensitivity of the system to the model parameters $\kappa^{'}$ and H. Finally, we present a more in-depth study of the phase properties exhibited at low amphiphile concentrations, where

conventional runs are unable to distinguish between amphiphiplic self assembly and simple phase coexistence.

3 Simulation results

3.1 Method of simulation and analysis

All of the simulations presented here were performed in the constant NVT ensemble using a standard MD algorithm [33, 34]. The Velocity Verlet algorithm was chosen for the integration step as it is known to be a robust integrator for relatively large time-step; a time-step of $\delta t = 0.0015$ was used here. The constant NVT ensemble was simulated by re-scaling the velocities at every time step using the Berendsen thermostat.

The starting configuration for each run was obtained by taking an orientationally isotropic configuration with 100% rod concentration and substituting rods by spheres until the required ratio was obtained. In doing this, care was taken to compensate for the differing volumes of the different particle shapes. This was achieved by running all systems at approximatively the same volume fraction. Considering each rod as a linear chain of spheres the volume of a rod can be approximated by

$$V_{rod} \approx \frac{\Pi}{6}\frac{l}{d}\sigma_0^3 = \frac{l}{d} \cdot V_{sph}. \tag{11}$$

Recalling that here $l/d = 3$, the total volume of particles in the system is:

$$V_{occ} \approx N_{sph} \cdot V_{sph} + N_{rod} \cdot 3V_{sph} = V_{sph} \cdot (N_{total} + 2N_{rod}). \tag{12}$$

Thus, the volume fraction can be expressed as:

$$V_f = \frac{V_{occ}}{V_{total}} = V_{sph} \cdot (\rho + 2C_{rod}). \tag{13}$$

Therefore, for each concentration, the box density was adjusted so as to achieve a volume

fraction of 0.44 which, at moderate temperatures, corresponds to a liquid phase for Lennard-Jones particles. Cubic box periodic boundary conditions, the minimum image convention and the Verlet neighbour list were employed. A spherical cut-off distance of $r_{cut} = 4.0\sigma_0$ was employed for all inter-particle potentials. The systems were quenched for $2 \times 10^6 \delta t$ from an isotropic configuration, initially equilibrated at high temperature, to a lower temperature of $T = 0.7$. It was found that this rapid quenching approach yielded the same self assembled structures as multi-step cooling sequences.

In order to perform further analysis on the resultant aggregates, a cluster identification algorithm was developed. In such an algorithm, when distinguishing between a non-aggregated particle or monomer and a particle belonging to a cluster, it is common for a simple cutoff distance, r_c, between particles to be used as criterion. For the amphiphilic systems considered here, however, the distance between the particle centres of mass, defined by $|\mathbf{r}_{ij}|$, proved poor at differentiating between monomers and aggregated particles. Rather, the distance $\left|\mathbf{r}'_{ij}\right|$ between the solvophobic ends of the rod particles was found to be a more robust indicator. Fig. 4 clearly illustrates this idea; essentially, two amphiphilic rods were judged to be aggregated if their solvophobic ends were in close proximity to each other.

At low rod concentrations the sites associated with the rods' solvophobic ends formed dense clouds of points inside each aggregate, and these could be identified using relatively small cutoff distances. Keeping this cutoff distance small proved useful since it helped to avoid nearby monomers (or particles from another aggregate) from being judged part of a given cluster. This cluster identification algorithm enabled calculation of the number of clusters present in each configuration. It also made it possible, by comparing the lists of particles belonging to each cluster at different timesteps, to track clusters through time. At low amphiphile concentrations, this analysis was performed using the rods only, as the solvent spheres were largely acting as a homogeneous bath. However, at high rod concentrations, cluster analysis on the spheres also proved informative, particularly for systems that formed inverse phases.

3.2 Variation of phase behaviour with concentration

A systematic series of exploratory simulations was performed to investigate the concentration dependance of the $H = 80\%$ and $\kappa' = 1/5$ system at a constant temperature of $T = 0.7$. To this end, ten rod-sphere mixtures were simulated using $N = 1024$ particles in total, the rod concentrations being 5%, 10%, 20%, 30%, 40%, 50%, 60%, 70%, 80%, 90%, by number.

The final configuration snapshots of the 2×10^6 timestep MD runs, shown in Fig. 5, display a wide range of phase behaviours. With increasing concentration, one can observe the self-assembly of spherical and cylindrical aggregates, lamellar phases, curved bilayers and inverse micellar phases. This sequence is in agreement with experimental phase diagrams and other simulations [**?**]. From low to high amphiphile concentration, the aggregates change from being positive curvature objects, *e.g.* micelles (Fig. 5(a)), to negative curvature objects, *e.g.* inverse micelles (Fig. 5(f)). The zero curvature state is represented by the lamellar phase (Fig. 5(c)) found at intermediate concentrations. Given the simplicity of the CG model employed here, the range of phases apparent from this initial survey for a single parameterisation is very encouraging.

To assess the behaviour of the model in more detail, we now consider the self-assembly mechanisms observed in the development of the configurations shown in Fig. 5. Specifically, using a cluster analysis approach, we track the histories of the aggregation processes observed. Principally, this is achieved by monitoring time series of the aggregate size and normalised principal moments of inertia (I_L, I_M and I_S) through each run.

Fig. 6 shows the evolution of the aggregate size and the principal moments of inertia of the largest aggregates found in the 5% and 10% amphiphile concentration systems. Fig. 6(a) clearly shows a three-stage process in which the main aggregate formed after only 50×10^3 steps and remained unchanged for about 150×10^3 steps after which other smaller aggregates coalesced with it almost simultaneously over a short period (about $10 \times 10^3 \delta t$). One can observe that the aggregate formed before 0.2×10^6 steps was nearly spherical as its moments of inertia are close to each other. When the other aggregates first joined the main one, the moment of inertia data

indicate a cylindrical shape which then rapidly reverted to being near-spherical again. Note that the time required for the aggregates to go back to being spherical was similar to that of the initial self-assembly from the isotropic configuration. At around 0.9×10^6 steps, another very small aggregate finally joined, leading to a single micelle-like aggregate.

Due to the small system size used here, it is not possible to establish, from this simulation, whether this result corresponds to a genuine micellar phase or if the system simply underwent a bulk phase separation as seen with other mixtures of rods and spheres [30, 31, 35]. Also, the structure of this aggregate and the associated self-assembly dynamics might have been affected by the periodic boundary conditions. These issues are investigated in greater detail in section 3.4 through the use of a significantly larger simulation performed at this rod concentration.

For the 10% system, the evolution of the size of the main aggregate again showed a rapid initial clustering that took place over about $50 \times 10^3 \delta t$ (Fig. 6(a)). In contrast to the 5% system, this self-assembly process took place in a single stage, presumably due to the higher concentration of rods. Also, the moment of inertia data indicate that the aggregate was only slightly cylindrical before, at $0.6 \times 10^6 \delta t$, it fused with its own image through the periodic boundaries. Following this self-fusion, the aggregate adopted the shape of a 'tubular' micelle. The fact that the original aggregate formed by this system remained stable for nearly $0.5 \times 10^6 \delta t$ before being 'trapped' by its own image strongly suggests that system size was an issue here. As such, the worm-like micellar aggregate apparent from Fig. 5(b) may not be a genuinely stable structure for this model parameterisation.

The time evolution of the 30% system is illustrated in Fig. 7 through configuration snapshots taken at significant steps in the development of the final lamellar bilayer arrangement. The first of these steps was the rapid aggregation of the amphiphiles into random aggregates in which the solvophobic regions were shielded from the solvent spheres. These aggregates then slowly arranged themselves and coalesced, leading to the formation of two bilayer-like aggregates which went on to fuse with themselves through the periodic boundary conditions. Following this, a series of slow local re-arrangements took place in which the bilayers freed themselves of pores

and various other defects. The corresponding histories of the principal moment of inertia and aggregate size data confirm this timeline: the largest aggregate at short times had a spherical shape, but it grew rapidly and became increasingly planar, this being the signature of the nascent bilayer. A sharp change is apparent in the aggregate shape at about 0.5×10^6 steps, which configuration snapshots confirm as corresponding to the bilayer merging with its own image through the boundary conditions. The associated decrease in the aggregate size was probably a consequence of the bilayer needing to become commensurate with the simulation box periodicity. We note that the process pathway just outlined shows a very strong similarities to that identified by Marrink et al. from their all-atom simulation study of bilayer formation [**?**]. Qualitatively, at least, this suggests that the neglect of intramolecular degrees of freedom in our model does not have a significant effect on self-assembly dynamics. While the stability of the planar bilayers obtained at the end of this run was likely enhanced by the periodic boudary conditions, there appears little evidence to suggest that the bilayers were reliant on those boundary conditions for their stability. Both the planar character of the growing aggregates and the fact that the bilayers formed at an angle to the box axes (and so were able to modify their effective areas) support the assertion that the planar bilayer was the stable phase at this concentration. Furthermore, similar bilayer arrangements were adopted in runs on systems with amphiphile concentrations of 20% and 40%.

On increasing the amphiphile concentration to 50-60% by number, the cluster-identification-based analysis route ceased to be particularly informative. Essentially, these systems formed bicontinuous, spongey networks in which all of the amphiphiles aggregated into relatively open, curved bilayer structures. These networks were found to form relatively quickly, but, despite repeated runs performed with different starting configurations, no specific mesoscale structure could be associated with these apparently rather random final structures.

At 70%, rod concentration the solvent domains appeared to cease to be continuous, shrinking so as to form solvent droplets surrounded by amphiphilic rods. Fig. 5(e) and Fig. 5(f) show the final configuration snapshots for the 70% and 90% systems at $T = 0.7$. To explore the

structural changes occurring in this concentration range, cluster analysis was performed on the spheres for the 70, 80 and 90% systems, as shown on Fig. 9. These plots clearly indicate the formation of stable sphere clusters for all three systems. However, for 70%, the number of clusters in the system slowly decays to unity, suggesting that the spheres *just* percolate at this concentration. Furthermore, the associated cluster size probability distribution function indicated a single cluster of about 300 spheres, whereas those for the 80% and 90% systems indicated average cluster sizes of 15 and 5, respectively. Thus, on increasing the amphiphile concentration above 70%, the structure adopted ceases to be bicontinuous and inverse phases are formed. These are characterised by water droplets encapsulated within amphiphile bilayers (i.e. the opposite of a normal micellar phase where surfactant droplets form in water).

3.3 Effect of molecular parameters on phase behaviour

In this section, we briefly survey the effect of the model paramters H and $\kappa^{'}$ on the system phase behaviour. The aim here is to determine the sensitivity of the model to changes in these interaction parameters.

3.3.1 Effect of H, the solvophilic to solvophobic balance

In order to assess the effect of the solvophilic to solvophobic ratio on the phase behaviour of these systems, a second series of simulations was performed at a range of amphiphile concentrations, but this time with the parameter H set to 50%. Other than this change in the headgroup size, the simulation procedures and parameters used were the same as those employed in the previous section. The results are summarised via the configuration snapshots shown in Fig. 10.

At 5% amphiphile concentration, a micelle-like phase was found, which remained stable up to 25% amphiphile concentration. The micelles obtained here were significantly different from that formed by the $H = 80\%$ system; they were smaller, more highly curved aggregates and were not as well defined. For rod concentration of 30% to 60%, bilayer structures were formed when the micelles start to join through the periodic boundary conditions. However, rather than

being lamellar, these systems were characterised by curvy and entangled intersecting bilayers. For amphiphile concentrations of 70% and above, inverse phases, similar to those obtained with the $H = 80\%$ system, were found.

In conclusion, decreasing H to 50% led to a sensible sequence of amphiphilic behaviour with increasing concentration. However, the number of different phases observed was significantly smaller than that seen for the $H = 80\%$ system. Furthermore, even when the same phases were formed, their properties (*e.g.* micelle structure, bilayer flexibility) were clearly different. These differences were consistent with the behaviour expected from increasing the amphiphilic headgroup size.

3.3.2 Effect of κ', the amphiphilic strength

The parameter κ' controls the strength of the anisotropy of the rod-sphere interaction, i.e. the hydration strength. To investigate the effect of this model parameter on system properties, an extended simulation was performed on an $N = 1024$ 10% rod system at constant temperature ($T = 0.7$) with H set to 50%. Within this run, the value of the amphiphilic strength was modified every 1.0×10^6 timesteps in the sequence $\kappa' = 1/5$, $\kappa' = 1/3$, $\kappa' = 1/2.5$ and finally $\kappa' = 1$ (where no amphiphilic behaviour should be expected).

The normalised principle moments of inertia of the largest aggregate formed in this system were monitored over the course of this run. These are shown in Fig. 11. From $t = 0\delta t$ to $t = 1.0 \times 10^6 \delta t$, ($\kappa' = 1/5$) these indicate the self-assembly of a near spherical aggregate from a random initial configuration. This is confirmed by the configuration snapshot on Fig. 12(a) which displays a multi-micellar arrangement of near-spherical aggregates.

At $t = 1.0 \times 10^6 \delta t$, the amphiphilic strength was switched to 1/3 and one can notice a repartitioning of the principal moments of inertia indicating a more cylindrical shape of the main aggregate in the system. As shown by the configuration snapshot of Fig. 12(b), here all the amphiphiles had aggregated into a single cluster with a cylindrical symmetry. This closed cylinder remained stable until the amphiphilic strength was reduced to 1/2.5 at $t = 2.0 \times 10^6 \delta t$.

Here, a similar change was found to that observed previously for the $H = 80\%$, $\kappa' = 1/5$ system at 10% rod concentration (recall Fig. 5(b) and Fig. 6(b)). Thus, the aggregate fused with itself through the periodic boundary conditions and formed a 'tubular' micelle (Fig. 12(c)). As before, this structure was clearly stabilised by this self-fusion as much less noise can be observed in its moment of inertia data. At $t = 3.0 \times 10^6 \delta t$, the amphiphilic strength was switched to unity which, in principle, should not promote amphiphilic behaviour as no anisotropy is present in the energy parameter of the rod-sphere potential. As expected, then, the previously observed structure collapsed soon after this final switch to give an isotropic mixture of rods and spheres (Fig. 12(d)).

This brief survey certainly suggests that the amphiphilic behaviour (i.e. the structure shape) exhibited by these systems is sensitive to the hydrophilic interaction strength: setting the hydrophilic strength $1/\kappa'$ closer to unity progressively reduces the curvature in the structure formed. The amphiphilic aggregates are surpisingly stable even at very low amphiphilic strength such as $\kappa' = 1/2.5$, and it is only when the amphiphilic strength is reduced to unity that the structure collapses completely.

3.4 Simulation of the micellar phase

At 5% amphiphile concentration, 1024 particle simulation performed using the $H = 80\%$, $\kappa' = 1/5$ parameterisation led to the formation of a single near-spherical aggregate. As discussed earlier, at that relatively small system size, it was not possible to determine whether this observation corresponded to phase separation or micelle formation. In order to address this issue, a larger system was required to give access to the longer length-scale properties of this system. To this end, a system of 8192 particles (containing 410 rods corresponding to a 5% system) was created by replicating eight images of the initial configuration of the 1024 particle system. This 8192 particle system was then run for 1×10^6 MD steps, all of the other simulation parameters being set to those used in the previous simulations. Configuration files were dumped every 1000 steps for post-simulation analysis.

Fig. 4 shows the final configuration snapshot obtained for this run. Here, one can observe multiple distinct assemblies (the solvent spheres are not shown for clarity) each of which is similar to the single aggregate observed in the 1024 particle system. These aggregates are all of similar size and shape and are also in equilibirum with monomers. Virtually no intermediate aggregate sizes can be seen on this snapshot. To check the equilibration of this 8192 particle system, the time evolution of the number of monomers was monitored throughout this run (see Fig. 4). From this analysis, one can observe that the monomer number attained a non-zero steady state value after 0.6×10^6 time steps, the early stage of the run being characterised by a rapid initial clustering of the particles. The qualitative form of this monomer-number graph was found to be largely independent of the cluster cut-off distance r_c, similar equilibration times being indicated for a range of r_c values.

Following the initial self-assembly process of 0.6×10^6 steps, a number of clusters had formed in equilibrium with these monomers. From the cluster-counting algorithm, a probability size distribution function $P(n)$, where n is the cluster size, was calculated. The form of this probably distribution was found to be strongly dependent on the cluster counting cut-off distance used. For large r_c (i.e. $\geq 1.20\sigma_0$), the algorithm tended to identify pairs of separate aggregates as single clusters, resulting in noisey distribution functions with a few sharp peaks. On the other hand, if the cutoff distance was set too small, no or very few clusters were identified and the distribution function just showed monotonic decay from a very high monomer peak. At the intermediate cutoff values ($r_c = 0.80\sigma_0$), smoother distribution functions were obtained, showing both a high monomer peak and a broad second peak centered on the aggregate preferred size or mean aggregation number (of ~ 25 in this system). This can be seen in Fig. 4, where the distribution function obtained by averaging over all configurations from $0.6 \times 10^6 < t < 1.0 \times 10^6$ is shown as $n \times P(n)$. The minimum found between the monomer and micellar peas demonstrates that clusters of intermediate size (i.e. sub-micellar aggregates) were less prevalent than monomers and micelles (confirming the earlier observation based on the configuration snapshot Fig. 4). The long tail in the $n \times P(n)$ data for $n > 40$ arose due to the occasional detection of large

assemblies. These occured due to events involving micelle fusion followed by fission, so that these large aggregates were only short-lived.

Fig. 4 shows the 3 principal moments of inertia averaged over the time window $0.6 \times 10^6 < t < 1.0 \times 10^6$ as a function of cluster size, n. By correlating this plot with the micelle size distribution function (Fig. 4), it can be seen that at the mean aggregation number, the micelles were at their most spherical - (I_l, I_m and I_s are at their closest to $\frac{1}{3}$). At larger n, these data become rather noisier, due to the worsening statistics, but they tend increasingly to the values expected for cylindrical micelle shape, consistent with these large assemblies being related to fusion and fission events.

4 Conclusion

In this study, a rod-sphere computer model has been developed based on a mixture of Gay-Berne and Lennard-Jones particles. In this, the rod-sphere potential has been adjusted in order to promote amphiphilic behaviour. Specifically, one end of the rod has been made strongly attractive to the solvent sphere, the other end being only weakly attractive.

From the simulations presented here, it seems that this model is suitable for studying the effects of molecular interaction parameters on a range of self-assembly processes. Molecular characteristics such as the solvophobic chain length and the solvophobic strength can be readily changed within this generic model and their effects on phase properties assessed. The range of phases accessible to this model is surprisingly large, given its simplicity, and the simulation timescales accessible appear more than adequate for phase stability to be established. We are not aware of any other model capable of exhibiting this range of phase behaviour from a single molecular parameterisation. It is also noteworthy that the self-assembly processes observed here are driven purely by the amphiphilic effect (modelled here by the dipolar symmetry in the rod-sphere interaction). This contests starkly with the 'solvent-free' amphiphile models employed in other recent studies of bilayers and vesicles [16, 36, 37].

Here, the effect of concentration has been studied for the parameter sets $H = 80\%$; $\kappa' = 1/5$

and $H = 50\%$; $\kappa^{'} = 1/5$. Then, the effect of varying the amphiphilic strength $\kappa^{'}$ has been examined at constant $H = 50\%$. While concentration has proved the main determinant of phase stability, $\kappa^{'}$ and H also play measurable roles. Little temperature dependance has been observed, other than to gain compositional isotropy by imposing high temperature values.

Due to the relatively low computational cost of this model and the fact that its particles cannot suffer from entanglements, it has proved possible to establish an equilibrated multi-micellar system. We shall consider the processes and properties found in such systems in a subsequent publication. Here we note that, like previous workers, we have been able to observe this self-assembly without recourse to a term representing solvent entropy. This is largely eplained by the relatively strong enthalpic head-solvent interaction used in this study. The results obtained here raise the prospect, though, of direct investigation of the relative importance of entropic and enthalpic contributions in micellar systems; entropic contributions could be incorporated into the current model in a number of ways (explicit or implicit). The roles played by such terms could then be assessed so as to investigate the fundamentals of the hydrodynamic effect in a systematic fashion.

Acknowledgements

We gratefully acknowledge the financial support of the MERI and EPSRC and Prof. Chris Care for useful discussion.

References

[1] R.G. Laughlin. *The aqueous phase beahviour of surfactants.* Academic Press Inc., San Diego, 1994.

[2] J. Israelachvili. *Intermolecular and Surface forces with applications to colloidal and biological systems.* Academic Press, 1991.

[3] R.G. Larson, L.E. Scriven, and H.T. Davis. Monte carlo simulation of model amphiphile-oil-water systems. *J. Chem. Phys.*, 83(5):2411–2420, 1985.

[4] J-C. Desplat and C.M. Care. A monte carlo simulation of the micellar phase of an amphiphile and solvent mixture. *Mol. Phys.*, 87(2):441–453, 1996.

[5] E. Lindahl and O. Edholm. Mesoscopic undulations and thickness fluctuations in lipid bilayers from moleclar dynamics simulations. *Biophys. J.*, 79:426–433, 2000.

[6] J-P. Mailet, V. Lachet, and P.V. Coveney. Large scale molecular dynamics simulations of self-assembly processes in short and long chain cationic surfactants. *Phys. Chem. Chem. Phys.*, 1:5277–5290, 1999.

[7] S.J. Marrink, A.H. De Vries, and A.E. Mark. Coarse grained model for semi-quantitative lipid simulations. *J. Phys. Chem. B*, 108:750–760, 2004.

[8] R. Goetz and R. Lipowsky. Computer simlations of bilayer membranes: self-assembly and interfacial tension. *J. Chem. Phys.*, 108(17):7397–7409, 1998.

[9] R. Goetz, G. Gompper, and R. Lipowsky. Mobility and elasticity of self-assembled membranes. *Phys. Rev. Lett.*, 82:221–224, 1999.

[10] B. Smit, P.A.J. Hilbers, and K. Esselink. Computer simulations of a water/oil interface in the presence of micelles. *Nature*, 348:624–625, 1990.

[11] S.J. Marrink and A.E. Mark. Molecular dynamics simulation of the formation, structure, and dynamics of small phospholipid vesicles. *J. Am. Chem. Soc.*, 125:15233–15242, 2003.

[12] D.P. Tieleman, H. Leontiadou, A.E. Mark, and S.J. Marrink. Simulation of pore formation in lipid bilayer by mechanical stress and electric field. *J. Am. Chem. Soc.*, 125:6382–6383, 2001.

[13] S.J. Marrink and A.E. Mark. the mechanism of vesicle fusion as revealed by molecular dynamics simulations. *J. Am. Chem. Soc.*, 125:11144–11145, 2003.

[14] J.C. Shelley, M.Y. Shelley, R.C. Reeder, S. Bandyopadhyay, and M.L. Klein. A coarse grain model for phospholipid simlutions. *J. Phys. Chem. B*, 105:4464–4470, 2001.

[15] J.C. Shelley, M.Y. Shelley, R.C. Reeder, S. Bandyopadhyay, P.B. Moore, and M.L. Klein. Simulations of phospholipids using a coarse grain model. *J. Phys. Chem. B*, 105:9785–9792, 2001.

[16] O. Farago. Water-free computer model for fluid bilayer membranes. *J. Chem. Phys.*, 119:596, 2003.

[17] I.R. Cooke, K. Kremer, and M. Deserno. Tunable generic model for fluid bilayer membranes. *Phys. Rev. E*, 72:011506, 2005.

[18] G. Brannigan and F.L.H. Brown. Solvent-free simulations of fluid membrane bilayers. *J. Chem. Phys.*, 120(2):1059–1071, 2004.

[19] J.G. Gay and B.J. Berne. Modification of the overlap potential to mimic a linear site-site potential. *J. Chem. Phys.*, 74(6):3316–3319, 1981.

[20] L. Whitehead, C. Edge, and J. Essex. Molecular dynamics simulation of the hydrocarbon region of a biomembrane using a reduced representation model. *J. Comp. Chem.*, 22:1622–1633, 2001.

[21] G. Ayton, S.G. Bardenhagen, P. McMurtry, D. Sulsky, and G.A. Voth. Interfacing continuum and molecular dynamics: An application to lipid bilayers. *J. Chem. Phys.*, 114(15):6913–6924, 2001.

[22] J.R. Gunn and K.A. Dawson. Microscopic model of amphiphilic assembly. *J. Chem. Phys.*, 91(10):6393–6403, 1989.

[23] J. Höpken, C. Pugh, W. Richtering, and M. Möller. *Makromol. Chem.*, 189:911–925, 1988.

[24] Y. Hayami and G.H. Findenegg. Surface crystallization and phase transitions of the adsorbed film of $f(cf_2)_{12}(ch_2)_{16}h$ at the surface of liquid. 1997.

[25] M.P. Turberg and J.E. Brady. Semifluotinated hydrocarbons: primitive surfactant molecules. *J. Am. Chem. Soc.*, 110:7797, 1988.

[26] P. Lo Nostro and S.H. Chen. Aggregation of a semifluorinated n-alkane in perfluorooctane. *J. Phys. Chem.*, 97:6535–6540, 1993.

[27] C.M. Care and D.J. Cleaver. Computer simulation of liquid crystals. *Rep. Prog. Phys.*, 68:2665–2700, 2005.

[28] G.R. Luckhurst and P.S.J. Simmonds. Computer simulation studies of anistropic systems. xxi. parametrization of the gay-berne mesogen. *Mol. Phys.*, 80:233, 1993.

[29] G.R. Luckhurst, R.A. Stephens, and R.W. Phippen. Computer simulation studies of anisotropic systems. xix mesophases formed by the gay-berne model mesogen. *Liqu. Crys.*, 8:451, 1990.

[30] D. Antypov and D.J. Cleaver. The role of attractive potentials in rod-sphere mixtures. *J. Chem. Phys.*, 120:10307, 2004.

[31] D. Antypov and D.J. Cleaver. The effect of spherical additives on a liquid crystal colloid. *J. Phys. Cond. Matt.*, 16:S1887, 2004.

[32] D.J. Cleaver, C.M. Care, M.P. Allen, and M.P. Neal. Extension and generalisation of the gay-berne potential. *Phys. Rev. E*, 54:559–567, 1996.

[33] M.P. Allen and D.J. Tildesley. *Computer simulation of liquids*. Oxford University Press, 1987.

[34] D. Frenkel and B. Smit. *Understanding molecular simulation. From algorithm to applications*. Academic Press Inc., U.S., 2001.

[35] D. Antypov and D.J. Cleaver. Orientational and phase-coexistence behaviour of hard rod-sphere mixtures. *Chem. Phys. Letts.*, 377:311, 2003.

[36] I.R. Cooke and M. Deserno. Solvent-free model for self-assembling fluid bilayer membranes: Stabilization of the fluid phase based on broad attractive tail potentials. *J. Chem. Phys.*, 123:224710, 2005.

[37] G. Brannigan, L.C.-L. Lin, and F.L.H. Brown. Implicit solvent simulation models for biomembranes. *Euro. Biophys. J.*, 35:104, 2006.

Figures

Fig. 1: Schematic diagram of a rod and a sphere.

Fig. 2: (a): Plot of the parameter C as a function of H for different values of $1/\kappa^{'}$ - (b): Energy functions for Antypov's rod-sphere interaction and two different parameterisations of the exponential model. The black dotted line corresponds to the constant $\epsilon_0 = -1$.

Fig. 3: Equipotential contour plot of the two models: (a) Exponential model for $\kappa^{'} = 1/5$ and H=50% - (b) Antypov's model for $\kappa^{'} = 1/5$.

Fig. 4: Diagram of two amphiphilic rods. The distance between particle is defined by the intermolecular vector $\mathbf{r_{ij}} = \mathbf{r_i} - \mathbf{r_j}$ and the distance between the two solvophobic ends is defined by the vector $\mathbf{r^{'}_{ij}} = \mathbf{r^{'}_i} - \mathbf{r^{'}_j}$ with $\mathbf{r^{'}_i} = \mathbf{r_i} - (\frac{\kappa}{\mathbf{2}}) \cdot \mathbf{\hat{u}_i}$.

Fig. 5: Configuration snapshots of 1024 particles system for different concentrations at $T = 0.7$. For figures (a), (b) and (c), the size of the solvent spheres has been reduced for clarity. Solvent spheres are in blue, solvophobic tails in green and solvophilic head groups in red.

Fig. 6: Evolution of the principal moments of inertia and size of the main aggregate in the (a) 5% and (b) 10% systems.

Fig. 7: Evolution of the 30% system in time.

Fig. 8: Evolution of the principal moments of inertia and size of the main aggregate in the 30% system.

Fig. 9: Evolution of the total numbers of sphere clusters in the high amphiphile concentration systems. Here, cluster analysis was performed on the solvent spheres with $r_c = 1.3$.

Fig. 10: Typical configuration snapshots of the H50K5 system for different rod concentration.

Fig. 11: Principal moments of inertia, I_L, I_M and I_S, of the largest cluster determined using $r_c = 0.9\sigma_0$. The regions (a), (b), (c) and (d) correspond to the $\kappa^{'}$ values and configurations snapshots shown on Fig. 12.

Fig. 12: Study of the effect of the rod-sphere interaction strength - 10% rod $H = 50\%$ system of 1024 particles at constant $T = 0.7$.

Fig. 13: Configuration snapshot after 10^6 MD steps with $N = 8192$ for 5% rod concentration at $T = 0.7$.

Fig. 14: Evolution of the number of monomers with time for a cut-off distance $r_c = 0.8\sigma_0$.

Fig. 15: Probability distribution $n \cdot P(n)$ vs. cluster size n for the 8912 particle system at 5% rod concentration and $T = 0.7$ averaged over $6 \times 10^5 \delta t < t < 10^6 \delta t$ for a cutoff distances of $r_c = 0.8\sigma_0$.

Fig. 16: Principle moments of inertia as a function of aggregate size for 8192 particle 5% system at $T = 0.7$

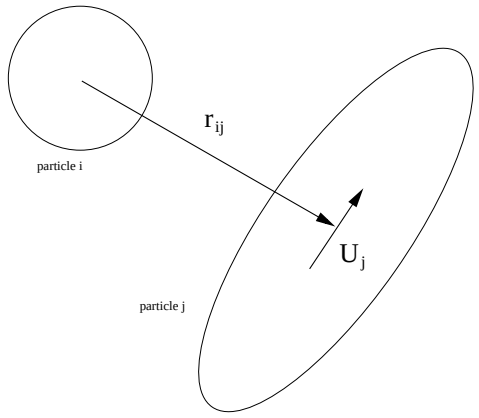

Figure 1:

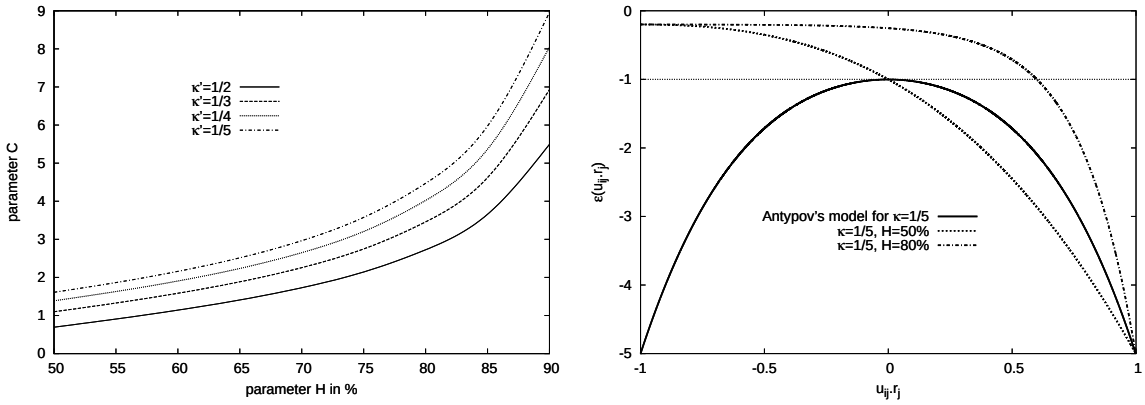
parameter C
parameter H in %
κ'=1/2
κ'=1/3
κ'=1/4
κ'=1/5
ε(u_ij,r_j)
u_ij.r_j
Antypov's model for κ=1/5
κ=1/5, H=50%
κ=1/5, H=80%

(a) (b)

Figure 2:

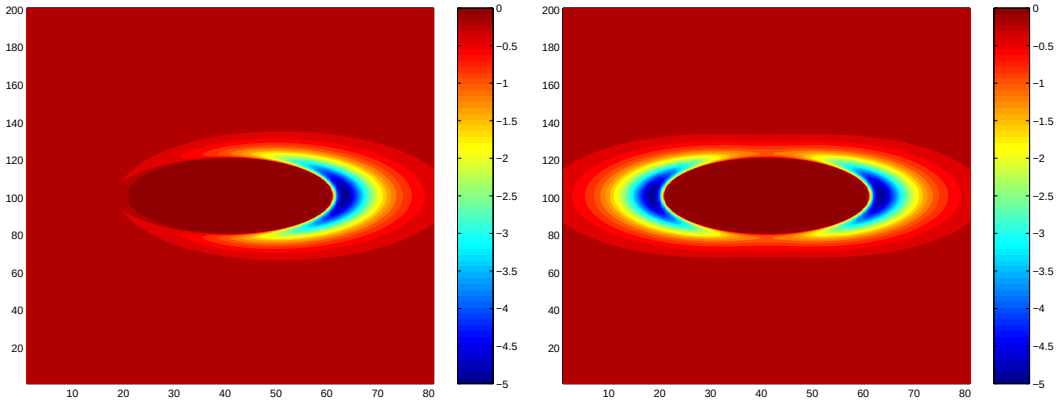
200
180
160
140
120
100
80
60
40
20
10
20
30
40
50
60
70
80
0
−0.5
−1
−1.5
−2
−2.5
−3
−3.5
−4
−4.5
−5

(a) (b)

Figure 3:

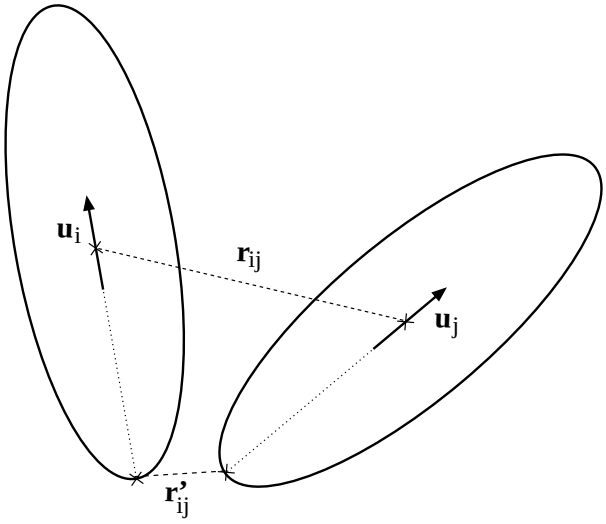

Figure 4:

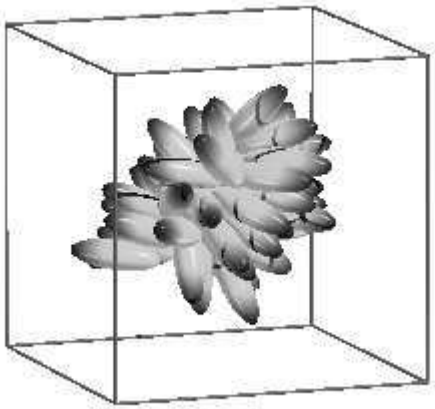

(a) 5% - ‘spherical’ micelle

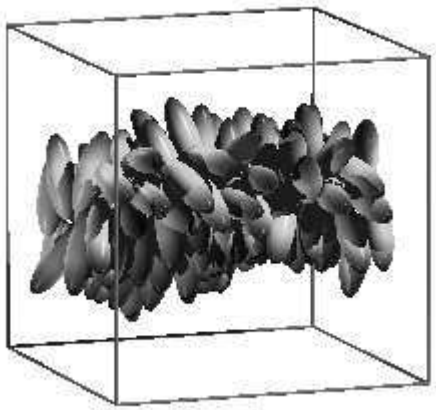

(b) 10% cylindrical micelle

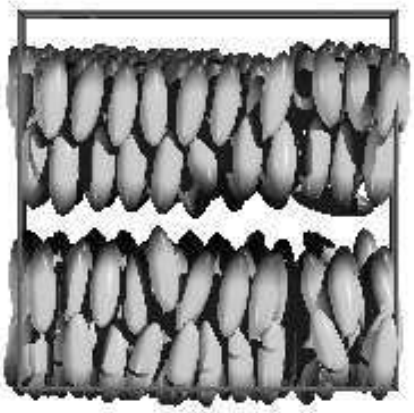

(c) 20%-40% lamellar phase

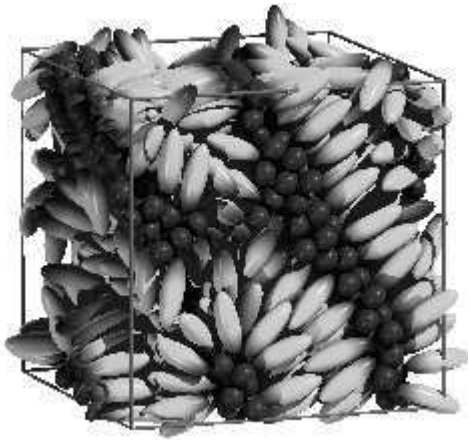

(d) 50%-70% sponge phase

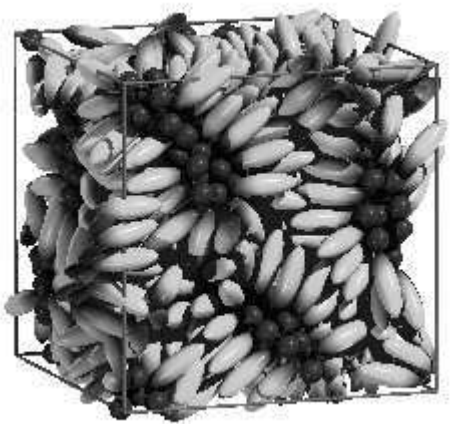

(e) 80% inverse cylindrical micelle

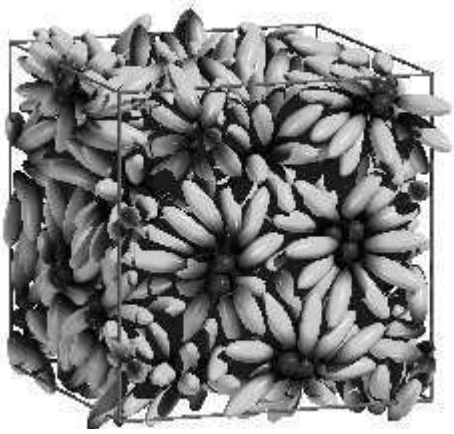

(f) 90% inverse spherical micelle

Figure 5:

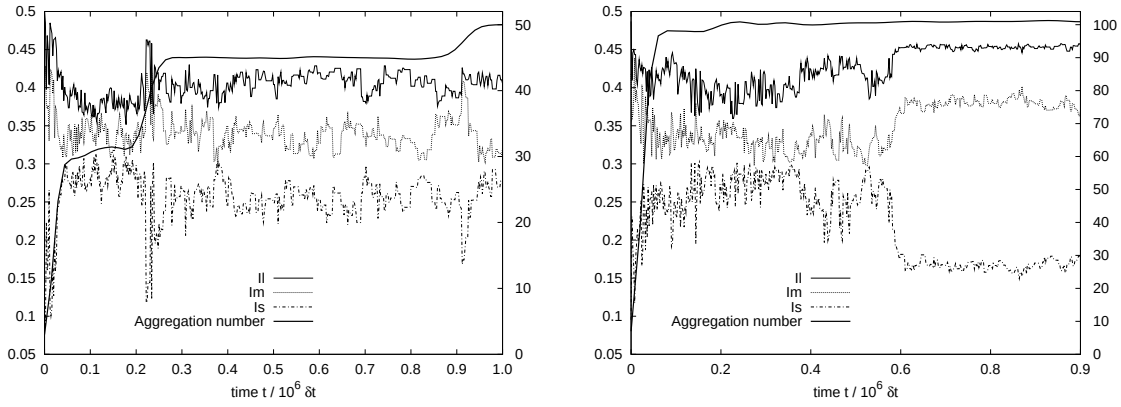
0.5
0.45
0.4
0.35
0.3
0.25
0.2
0.15
0.1
0.05
0
0.1
0.2
0.3
0.4
0.5
0.6
0.7
0.8
0.9
1.0
50
40
30
20
10
0
Il
Im
Is
Aggregation number
time t / 10^6 δt
0.5
0.45
0.4
0.35
0.3
0.25
0.2
0.15
0.1
0.05
0
0.2
0.4
0.6
0.8
0.9
100
90
80
70
60
50
40
30
20
10
0
Il
Im
Is
Aggregation number
time t / 10^6 δt

(a) (b)

Figure 6:

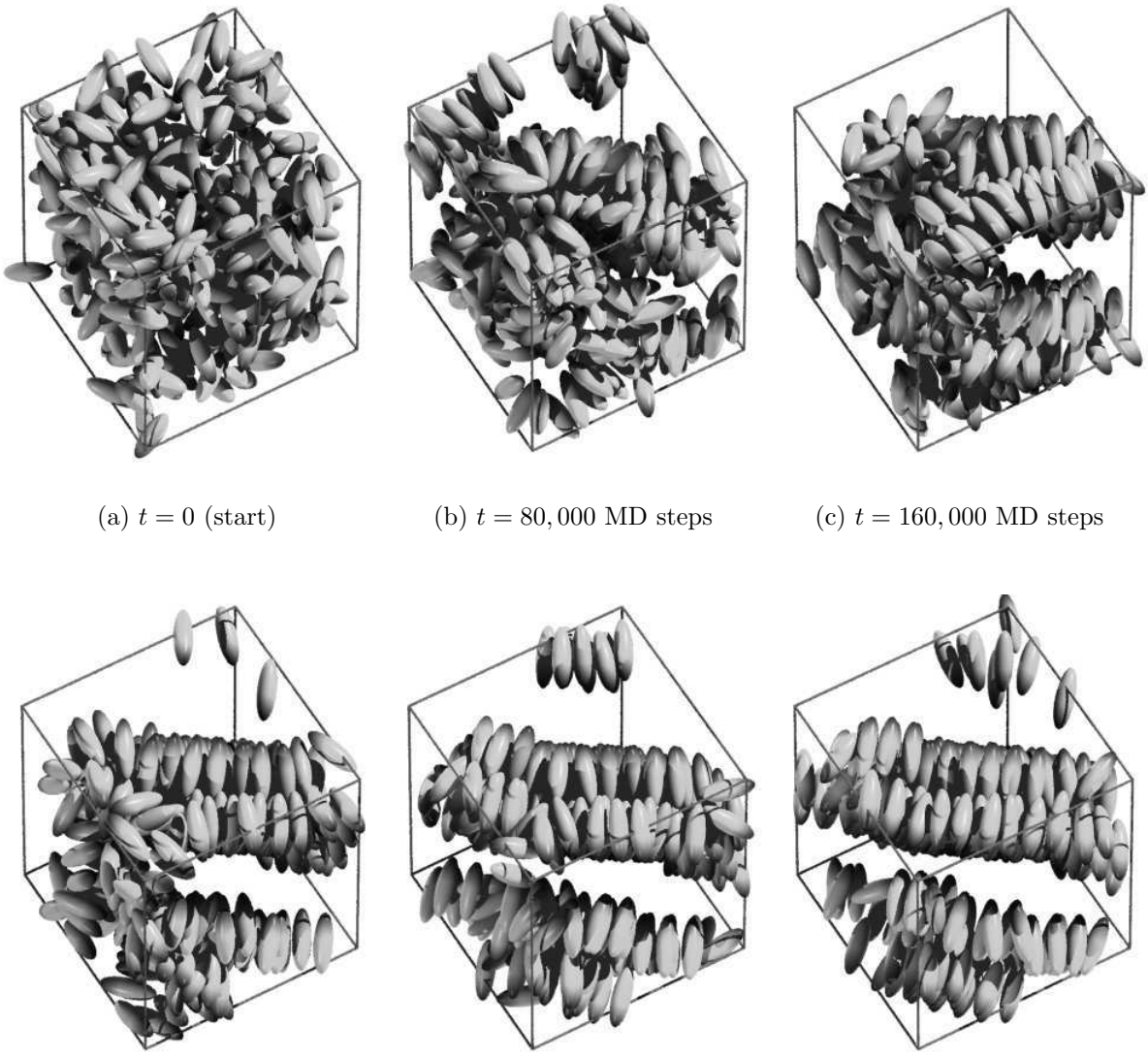

(a) $t = 0$ (start)

(b) $t = 80,000$ MD steps

(c) $t = 160,000$ MD steps

(d) $t = 240,000$ MD steps

(e) $t = 320,000$ MD steps

(f) $t = 400,000$ MD steps

Figure 7:

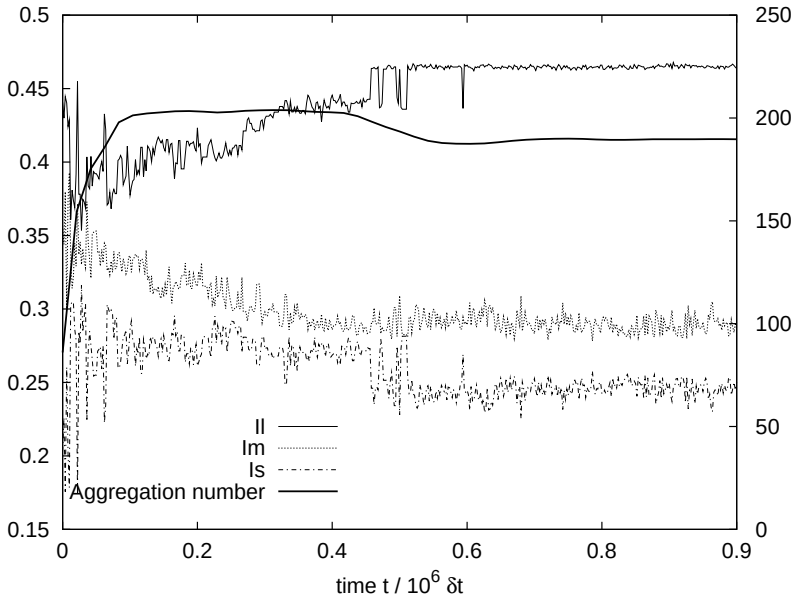
0.5
0.45
0.4
0.35
0.3
0.25
0.2
0.15
250
200
150
100
50
0
0
0.2
0.4
0.6
0.8
0.9
Il
Im
Is
Aggregation number
time t / 10^6 δt

Figure 8:

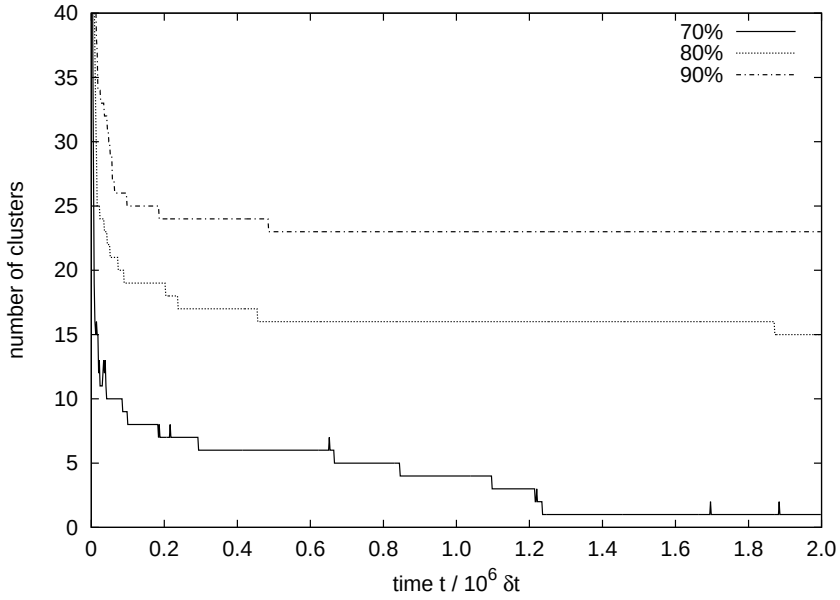
70%
80%
90%
number of clusters
time t / 10^6 δt
0
5
10
15
20
25
30
35
40
0
0.2
0.4
0.6
0.8
1.0
1.2
1.4
1.6
1.8
2.0

Figure 9:

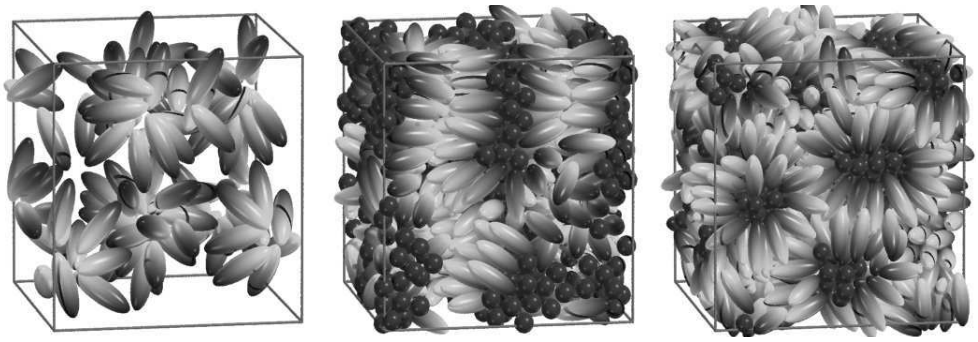

(a) 5 to 30%

(b) 40 to 60%

(c) 70 to 90%

Figure 10:

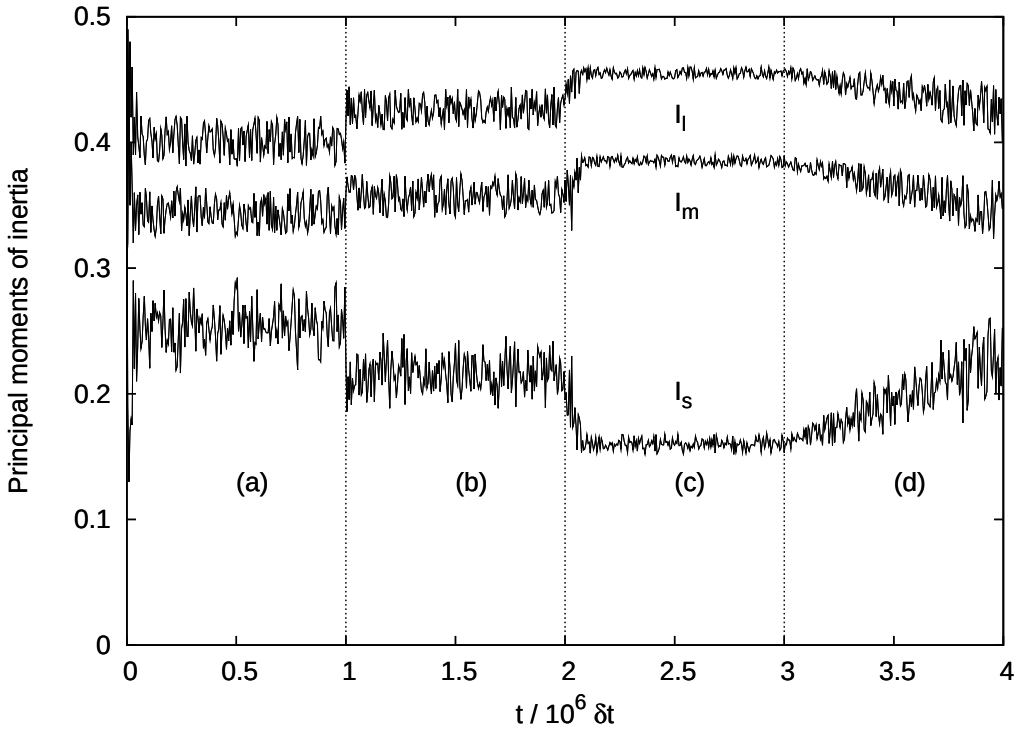
Principal moments of inertia
t / 10^6 δt
I_l
I_m
I_s
(a)
(b)
(c)
(d)
0
0.1
0.2
0.3
0.4
0.5
0
0.5
1
1.5
2
2.5
3
3.5
4

Figure 11:

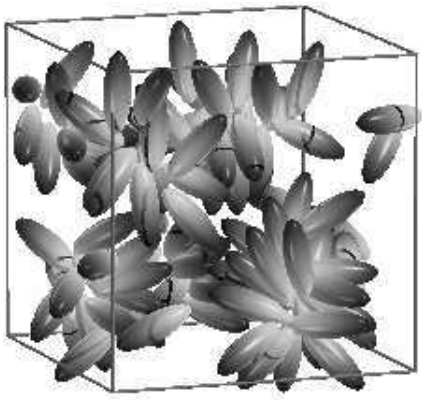

(a) $1/\kappa^{'} = 5.0$ - micelles

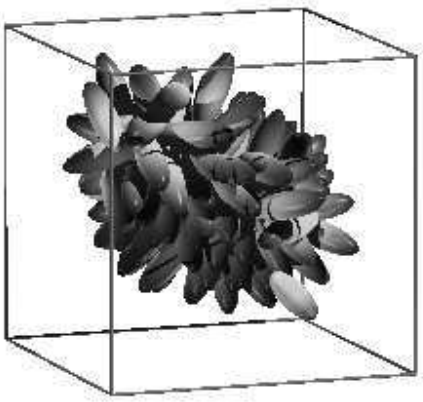

(b) $1/\kappa^{'} = 3.0$ - cylindrical micelle

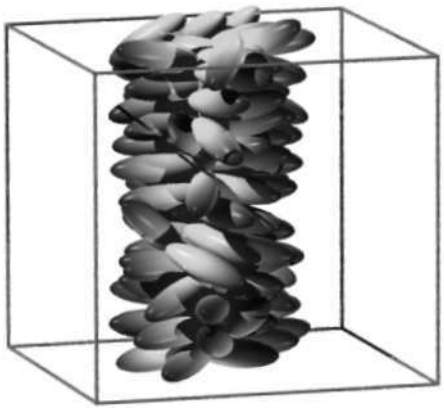

(c) $1/\kappa^{'} = 2.5$ - rod-shaped aggregate

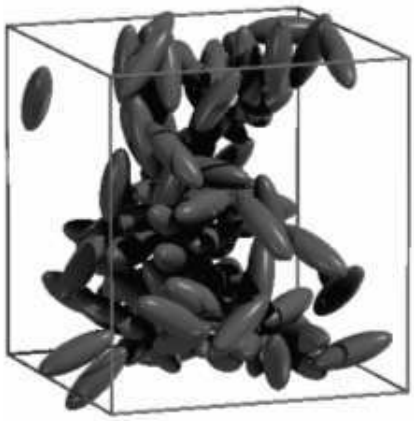

(d) $1/\kappa^{'} = 1.0$ - isotropic structure

Figure 12:

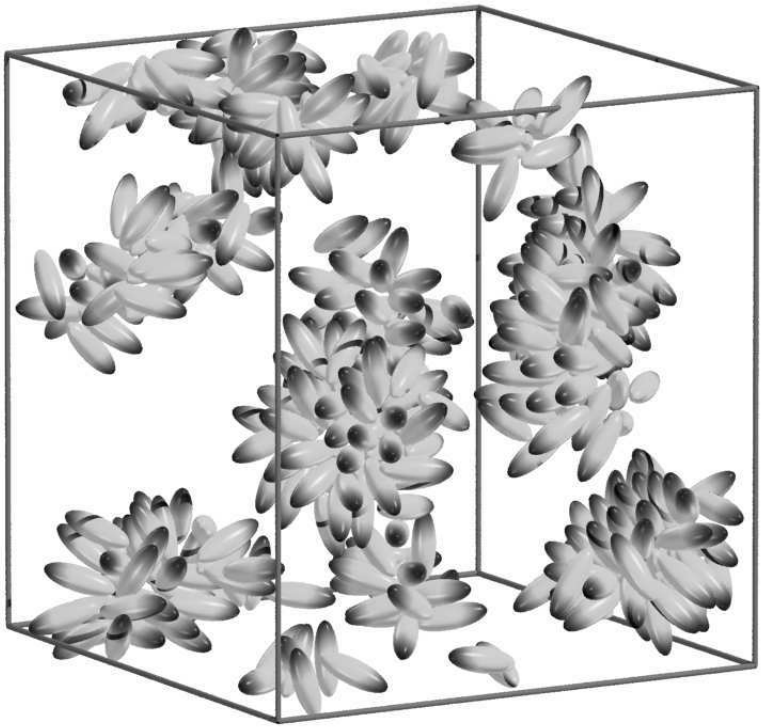

Figure 13:

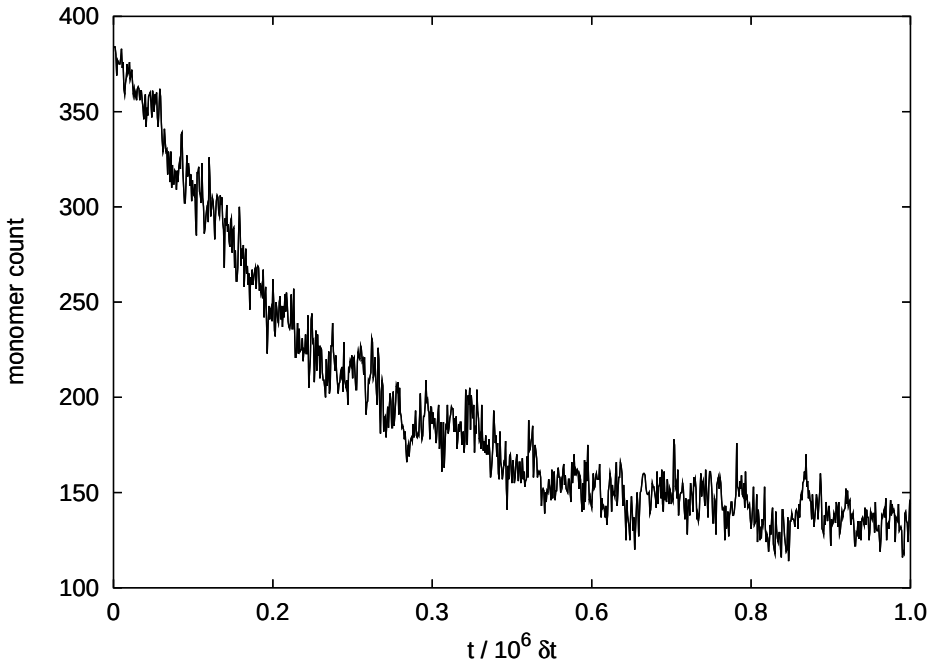
400
350
300
250
200
150
100
monomer count
0
0.2
0.3
0.6
0.8
1.0
t / 10^6 δt

Figure 14:

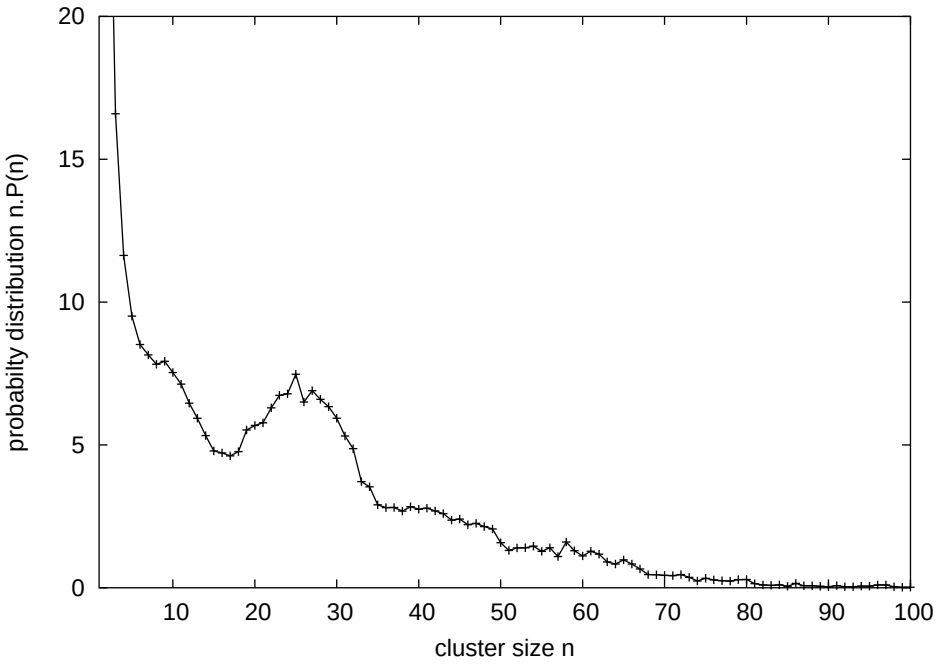
probabilty distribution n.P(n)
cluster size n
0
5
10
15
20
10
20
30
40
50
60
70
80
90
100

Figure 15:

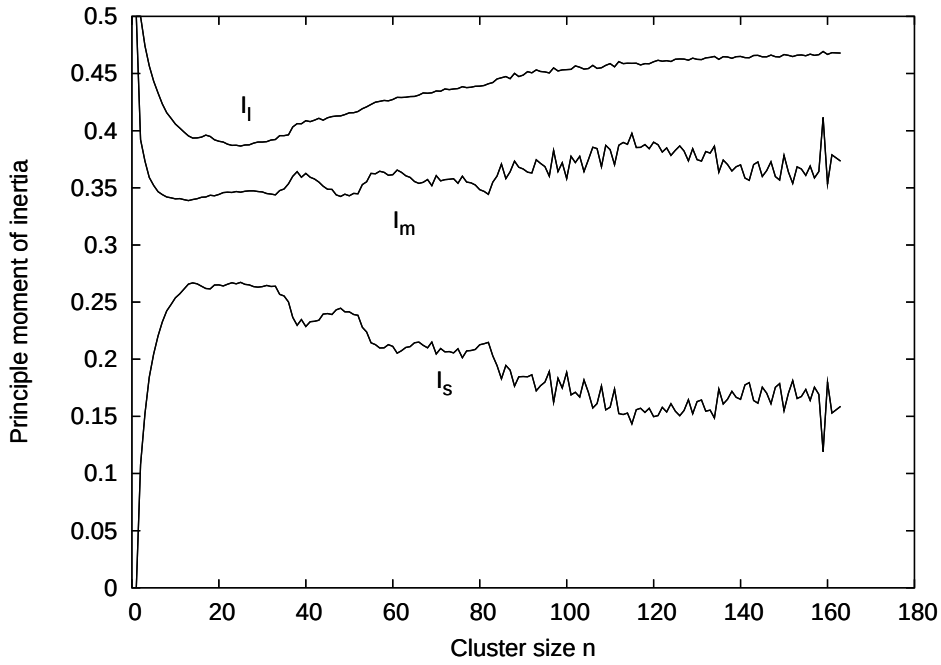
Principle moment of inertia
Cluster size n
I_l
I_m
I_s
0
0.05
0.1
0.15
0.2
0.25
0.3
0.35
0.4
0.45
0.5
0
20
40
60
80
100
120
140
160
180

Figure 16: